ISSN 1330-3651 (Print), ISSN 1848-6339 (Online)
https://doi.org/10.17559/TV-20230413000528
Original scientific paper

The Sand Removal Performance and Erosion Characteristics of Shale Gas Wellhead Desander

Jian ZHANG, Chang LIU, Dong LIN, Jian GAO, Changchao QI, Jun JIANG, Bo KOU, Shanbi PENG*

Abstract: In the process of shale gas extraction, fracturing technology is often used, and the extracted gas contains large amounts of sand, resulting in the risk of blockage and erosion of surface gathering equipment, which seriously affects safe production. To address this problem, this paper presents a numerical study of the sand removal performance and erosion characteristics of the filter desander used in Sichuan shale gas fields under different operating conditions (flow velocity, sand mass flow rate, operating pressure, and sand particle size) using CFD method. The results show that the increase of shale gas velocity is not conducive to the efficient operation of the filter desander. So the flow velocity should be controlled within 10 m/s as much as possible to avoid the rapid drawdown of separation efficiency and overly high erosion rate. When the sand size increases from 10μm to 100μm, the erosion area of the filter desander changes to sheet-like distribution, and the separation efficiency increases to 85%, a 2.3-fold increase. In addition, the change in operating pressure has a relatively small impact on the erosion wear of the desander.

Keywords: desander; erosion; separation efficiency; numerical simulation; shale gas

1 INTRODUCTION

Currently, with the promotion of "carbon neutral", the world has entered a critical period of energy transition, and the shift from fossil energy to new energy development has become an inevitable trend [1-4]. As an unconventional natural gas, shale gas has the characteristics of low pollution, high efficiency, and large reserves. At present, fracturing technology is often used in shale gas exploitation. The fracturing flow back fluid contains sand and other solid impurities, causing blockage and erosion of shale gas surface gathering equipment, which may lead to equipment and pipeline failure in serious cases and affect the safe production of gas field exploitation [5].

Shale gas wellheads in Sichuan mainly use filter desander to remove solid impurities such as sand. Fig. 1 is the structure of this device. During the operation process of the desander, the solid sand in the extracted gas will be blocked by the baffle and filter screen when passing through the desander, thus achieving the purpose of gas-solid separation. For the shale gas desander, separation efficiency is an important index to estimate its sand removal performance, which directly determines the safety and stability of gas field exploitation.

Figure 1 Filter desander

The filter desander is subject to severe erosion wear, as seen in Fig. 2. Over time, the cartridge filter will be broken through by solid sand, thus failing to work. At the same time, due to the wide parameters range of field operation, the separation effect cannot meet the production requirements, and the downstream separator will still be eroded by large amounts of sand.

(a) before erosion

(b) after erosion

Figure 2 Comparison between the desander cartridge filter before and after erosion

Therefore, it is necessary to study the sand removal performance and erosion characteristics of this equipment to clarify its reasonable operating conditions so that the filter desander can keep working efficiently. In recent years, scholars have carried out many studies on the sand removal performance of desanders, as shown in Tab. 1.

Table 1 Literature investigation on desander's sand removal performance in recent years

Research subjects	Achievement and discussion	Researchers
Heavy oil desander	1. A new type of sand removal device that can significantly improve separation efficiency and reliability is proposed, extending the service life of downstream equipment. 2. When the particle concentration increases, the separation efficiency may decrease. And the opposite is true when the particle size increases.	Feng et al., 2012 [6]
Hydroclone	By changing the inlet of the desander to multiple inlets and reducing the inlet width, the high kinetic energy fluid can be retained in the cylinder for a longer period of time, thereby improving the desander's sand removal performance.	Hwang et al., 2013 [7]
Cyclone desander	The tangential velocity increases as the velocity and inlet height increase, and the separation efficiency also increases, but an overly large inlet height will cause a reduction of separation efficiency.	Zhang et al., 2018 [8]
Cyclone separator	The pressure drop of the desander is not affected by the particle size, but like the separation efficiency, it also increases gradually as the flow velocity increases.	Masoumeh et al., 2019 [9]
Hydroclone	1. Under the separation effect of the desander, the aggregation phenomenon of microspheres will occur. 2. As the sand content increases, the particles will interact with each other, resulting in a decrease in separation efficiency. This phenomenon is especially obvious when the sand content exceeds 5%.	Alves et al., 2020 [10]
Filter desander	The sand kinetic energy increases as the gas velocity increases, so the sand trajectory in the desander under high-velocity operating conditions will be more turbulent, and their movement time and range of motion will be more extensive, resulting in a reduction of separation efficiency.	Peng et al., 2020 [11]
Horizontal desander	1. The trajectory of sand is related to its sand size. The larger the sand size, the smaller the displacement the particle moves downstream. 2. The physical properties of the fluid will change with the operating temperature and pressure of the desander, causing a fluctuating separation efficiency.	Basyouny, 2022 [12]

Table 2 The research status of desander erosion

Research subjects	Achievement and discussion	Researchers
Cyclone desander	1. The erosion rate increases gradually as the flow velocity increases, but it decreases with the increase of the solid loading ratio, especially when the flow velocity is above 30m/s. 2. When the buffering effect occurs, the particles will collide with each other, causing energy loss, thus avoiding the direct collision between the particles and the wall.	Sedrez et al., 2017 [16]
Cyclone desander	1. The larger the particle size, the more severe the erosion will be, for reasons such as higher centrifugal forces, longer movement times, and higher Stokes numbers. 2. When the surface roughness of the wall changes, the angle and speed of the particles hitting the wall of the desander will be affected, resulting in a change in the erosion characteristics of the desander.	Tofighian et al., 2020 [17]
Vertical separator	1. The erosion area at the separator wall changes as the flow velocity changes. 2. When the shale gas velocity and particle size increase, the erosion rate at the baffle also rises continuously.	Liu et al., 2021 [18]
Shale gas desander	1. The sand removal performance and erosion characteristics of shale gas desander change continuously with the change of structure size. 2. The erosion rate grows slowly in the range of 2 m/s ~ 10 m/s, while the erosion wear will rise significantly after exceeding 10 m/s.	Liu et al, 2022 [19]
Cyclone desander	1. The increase in inlet width and flow velocity will make the pressure loss of the desander rise significantly, but basically, the separation efficiency does not fluctuate. 2. The trajectory of sand particles is closely related to the distribution of the erosion area of the desander, and the existence of the "dust ring" will aggravate the erosion situation.	Liu et al., 2022 [20]
Cyclone desander	1. The erosion of sand particles on the wall of the desander will change the stability of the flow field, and as the process proceeds, the tangential velocity at the cone end decreases, increasing the probability of particles entering the internal cyclonic flow. 2. The local erosion of the wall of the desander will cause changes in the structure of the equipment, which affects the turbulence intensity and secondary flow of the airflow. More importantly, the sand removal performance and pressure loss will be reduced as a result.	Zhang et al., 2023 [21]

Up to now, scholars have conducted many studies of the separation performance, but there is still little research on erosion. Admittedly, this is closely related to the difficulty of the erosion experiments on desanders. With the rapid development of computer science, the application of Computational Fluid Dynamics (CFD) to erosion research has gradually become a trend [13-15]. This paper retrieved the CFD studies of desander erosion in recent years, and the summary is shown in Tab. 2.

In summary, most of the studies focus on the analysis and discussion of the sand removal performance and pressure loss of desanders and have proposed various methods for structural improvement. However, it can be seen from the above literature that as an important piece of equipment in the shale gas industry, filter desander has received little attention from scholars, and studies on their erosion studies are even more scarce. In view of the above reasons, this paper will analyse the sand removal performance and erosion characteristics of filter desander under different operating conditions to clarify the reasonable operating conditions and failure-prone locations of filter desanders, so that they can maintain efficient operation and provide technical guidance for field inspection at the same time.

In the second part, the turbulence model and erosion model are established, and the three-dimensional model of the filter desander is built by investigating the relevant parameters of existing desanders in Sichuan. In the third part, based on Ansys FLUENT, a hydrodynamics simulation software, the velocity and pressure fields inside the desander are analysed. Then, the effects of inlet velocity, sand mass flow, operating pressure, and sand size on the separation efficiency and erosion wear of the desander are further analysed, and a reasonable range of operating parameters is given.

2 MODEL AND METHOD

2.1 Mathematical Models

2.1.1 Continuity Equation

It is assumed that the shale gas is an incompressible ideal fluid in a turbulent state. Based on this assumption, the continuity equation is shown in Eq. (1):

$$\frac{\partial(\rho u_i)}{\partial x_i} = 0 \tag{1}$$

where, u_i is the average flow velocity of shale gas; x_i is the location.

2.1.2 Turbulence Equations

After the shale gas enters the filter desander, the fluid motion at the filter screen and the exhaust pipe are complex and variable, so the Realizable *k-ε* model is most applicable.

Turbulent kinetic energy *k* equation:

$$\frac{\partial(\rho k)}{\partial t} + \frac{\partial(\rho k u_i)}{\partial x_i} = \frac{\partial}{\partial x_j}\left[\left(\mu + \frac{\mu_t}{\sigma_k}\right)\frac{\partial k}{\partial x_j}\right] + G_k - \rho\varepsilon \tag{2}$$

Turbulence dissipation rate ε equation

$$\frac{\partial(\rho\varepsilon)}{\partial t} + \frac{\partial(\rho\varepsilon u_j)}{\partial x_j} = \frac{\partial}{\partial x_j}\left[\left(\mu + \frac{\mu_t}{\sigma_\varepsilon}\right)\frac{\partial \varepsilon}{\partial x_j}\right] + \rho C_1 S_\varepsilon - \rho C_2 \frac{\varepsilon^2}{k + \sqrt{\nu\varepsilon}} \tag{3}$$

Turbulent viscosity μ is represented by *k* and ε:

$$\mu_t = \rho C_\mu \frac{k^2}{\varepsilon} \tag{4}$$

C_μ in Eq. (4) is constant in the Standard k-ε model, but to better account for the swirling effect, the value in the Realizable *k-ε* model is determined by the following equation.

$$C_\mu = \frac{1}{A_0 + A_s U^* \frac{k}{\varepsilon}} \tag{5}$$

where, $U^* = \sqrt{S_{ij}S_{ij} + \Omega_{ij}^* \Omega_{ij}^*}$, $\Omega_{ij}^* = \Omega_{ij} - 2\varepsilon_{ijk}\omega_k$, $\Omega_{ij} = \bar{\Omega}_{ij} - 2\varepsilon_{ijk}\omega_k$, $A_0 = 4.04$, $A_s = \sqrt{6}\cos\phi$, $\bar{\Omega}_{ij}$ is the average rotation rate, whose value is obtained in a coordinate system rotated with angular velocity ω_k .

2.1.3 Discrete Phase Model

Considering the movement of sand carrying airflow in the filter desander, this paper simulates the flow field of gas-solid two-phase flow in the filter desander by the DPM model with the Euler-Lagrange method, and the motion equation of sand is solved to realize the particles' trajectory tracking control [22-24]. The equation of motion is:

$$\frac{\mathrm{d}u_p}{\mathrm{d}t} = F_D(u - u_p) + \frac{g(\rho_p - \rho)}{\rho_p} + F_y \tag{6}$$

$$F_D = \frac{18\mu}{\rho_p d_p^2}\frac{C_D Re}{24} \tag{7}$$

where, u is the gas velocity, m/s; u_p is sand velocity, m/s; *Fy* is other forms of forces in the *Y*-direction; μ is hydrodynamic viscosity, Pa·s; *dp* is sand diameter, m; C_D is drag force; *Re* is the relative Reynolds number (Reynolds number of sand).

2.1.4 Erosion Prediction Model

Oka et al. [25] proposed the Oka erosion prediction model in 2005, which is considered one of the best erosion models with universality [26]. Its expressions are as follows:

$$E = E_{90}\left(\frac{V}{V_{\text{ref}}}\right)^{k2}\left(\frac{d}{d_{\text{ref}}}\right)^{k3} f(\alpha) \tag{8}$$

$$f(\alpha) = (\sin\alpha)^{n1}\left(1 + H_v(1 - \sin\alpha)\right)^{n2} \tag{9}$$

where, E_{90} is the reference values of the target at 90°, kg/m^3; V is the particle impact velocity, m/s; V_{ref} is the relative particle impact velocity with the target, m/s; *k2, k*3 are the velocity and sand size index; α is the impact angle of the sand; $f(\alpha)$ is the impact angle function of the sand; n_1, n_2 are the impact angle function constants. Since the material selected in this paper is carbon steel, the corresponding parameters are shown in Tab. 3 [19]:

Table 3 Common parameter values of Oka equation

Object	E_{90}	H_V / GPa	n_1	n_2	*k*2	*k*3	d_{ref} / μm	V_{ref} / m/s
Parameter	6.15e^{-4}	1.8	0.8	1.3	2.35	0.19	326	104

2.2 Physical Model

2.2.1 The Three-Dimensional Model of Desander

By investigating the desander in Sichuan shale gas fields, we found the size of the desander is DN 300×1200. Considering that the numerical simulation ignores the wall thickness of the geometry model, the diameter of the desander is taken to be 290 mm and the total height is 1150 mm. The corresponding structural parameters are shown in Tab. 4. The 3D calculation model and grid of the filter desander were generated by ANSYS software, as shown in Fig. 3.

To facilitate the subsequent erosion studies and flow field analyses, a total of seven planes were selected and three data extraction lines were set up, as shown in Fig. 4.

Table 4 Geometry model parameters of the desander

Parameters	Cylinder diameter D_1	Inlet diameter d_1	Entrance length L_1	Cylinder height H_1	Exhaust pipe diameter D_2	The length of the exhaust pipe L_2	The height of the circular baffle H_2	The height of the filter screen H_3
Size / mm	290	84	100	1100	84	100	300	300

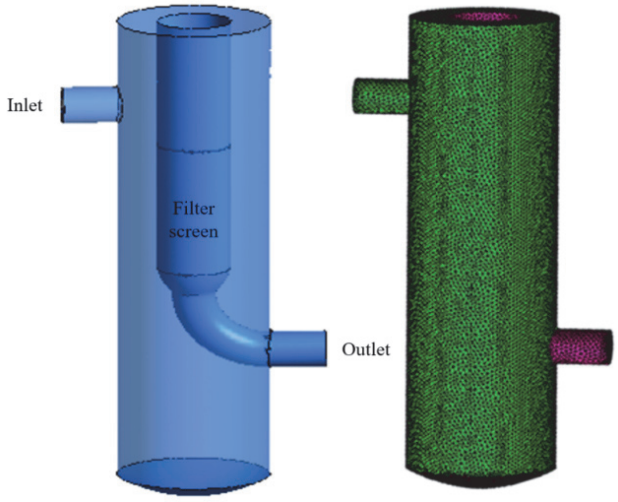

Figure 3 The structural representation of filter desander structure

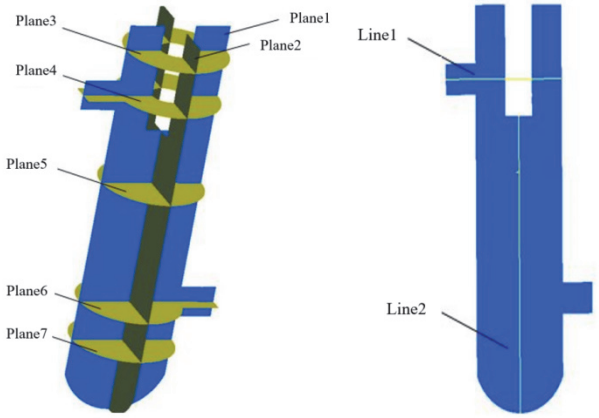

(a) Plane extraction diagram (b) Data extraction line distribution diagram

Figure 4 Plane extraction of desanders and data extraction line distribution

2.2.2 Grid Independence Test

The model and grid of the desander were generated by the ANSYS ICEM software, and the local refinement of the parts such as the exhaust elbow was performed. Considering the complex internal structure of the desander, this article adopts unstructured grids for grid division. The velocity inlet was used for the inlet and the pressure outlet was selected for the gas phase outlet, while the dust collector at the bottom was in trap mode. The inlet velocity is 6m/s, the outlet pressure is 3.0 MPa, the sand volume is 10kg/d, and the sand particles are using R-R distribution, which distribution range is 10 ~ 100 μm. The separation efficiency of the desander is used as the reference index for the grid independence test.

Fig. 5 shows that when the grid number reaches 634535, the separation efficiency of the desander no longer fluctuates significantly with the increase of the grid number. Therefore, it is considered that the independence requirement has been met when the grid number is 634535, so this model is taken as the calculation model.

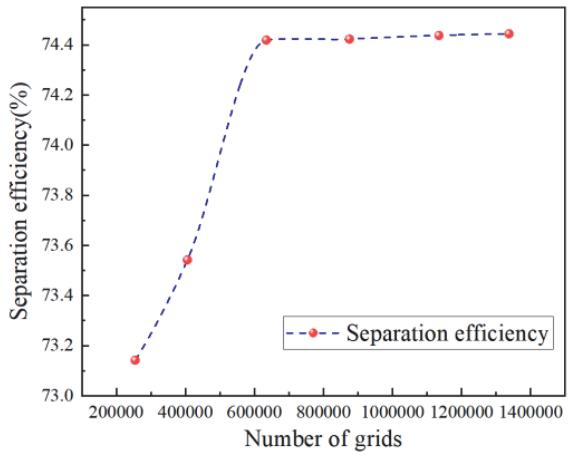

Figure 5 The grid independence test of filter desander

3 RESULTS AND DISCUSSION

3.1 Desander Two-Phase Flow Field Analysis

To better analyze the effect of shale gas on the sand particles in the dispersed phase inside the shale gas, numerical simulations were conducted for the operating condition with a velocity of 6 m/s and outlet pressure of 3.0 MPa, and the velocity and pressure distribution of gas-solid two-phase inside the desander were analyzed and discussed, as shown in Figs. 6 to 8.

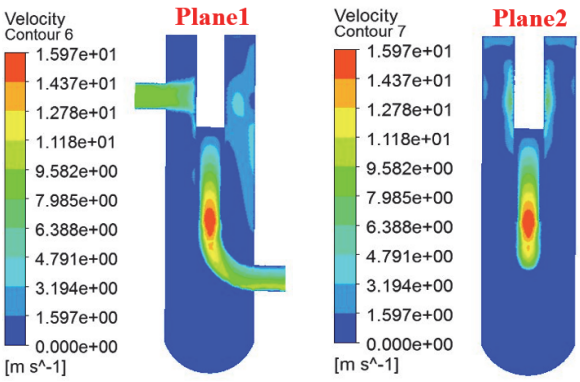

Figure 6 Velocity cloud images of plane 1 and plane 2

Fig. 6 shows the velocity distribution cloud images of plane 1 and plane 2. The velocity flow field inside the whole desander is quite turbulent. After entering the desander, the velocity of the sand-carrying flow in the inlet section remains the same. However, the shale gas velocity decreases significantly after encountering the inlet cylindrical baffle. The flow velocity in the outlet section increases significantly due to the reduction of the flow area.

As shown in Fig. 7, the flow is obstructed by the circular baffle after entering the desander, and part of the fluid performs tangential motion along the baffle, and the velocity is gradually decreasing. On the other side of the baffle, the two separated fluids meet and perform reentry movement. At the same time, the flow is restrained by the top and wall of the desander, thus forming a velocity field with a low velocity in the middle and a higher velocity on the inside and outside.

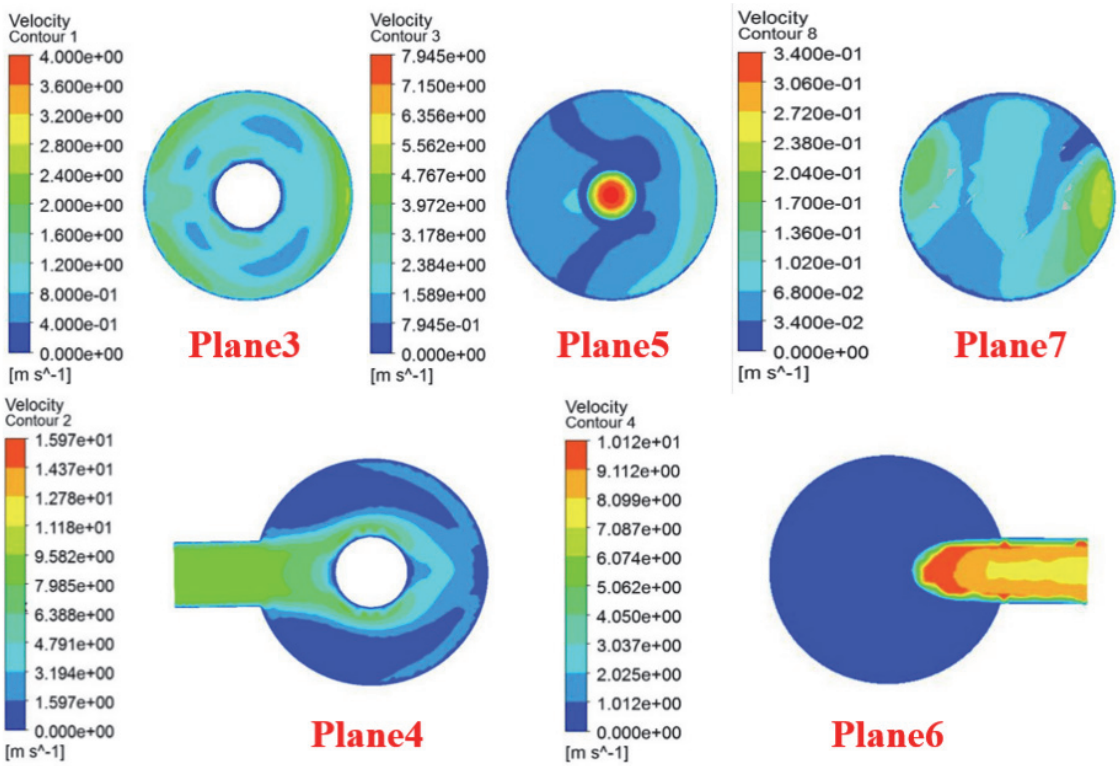

Figure 7 Velocity cloud images of different height planes

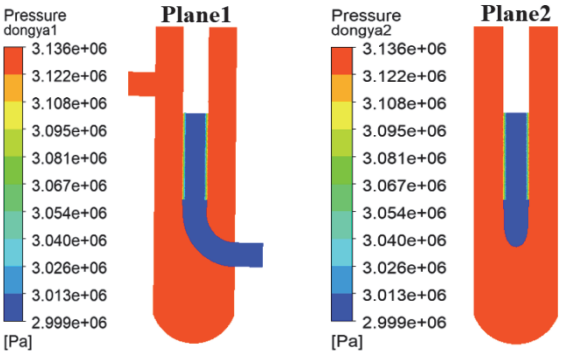

Figure 8 Pressure cloud images of plane 1 and plane 2

Plane 5 is the filter screen. There is a significant decrease in the velocity of the fluid as it passes through the filter screen. And inside the filter screen, there is a small increase in flow velocity because of the reduction of the flow area. The velocity distribution in plane 7 indicates that the shale gas performs a swirling motion at the bottom of the desander and generates the maximum velocity in the local area.

Fig. 8 shows the pressure distribution in the $X = 0$ and $Y = 0$ sections of the desander. The pressure is symmetrically distributed inside the desander about the axis, and the gas pressure reaches the minimum value inside the filter screen. The reason is that the flow field inside the desander is chaotic and the velocity direction keeps changing, so the pressure outside the filter screen is almost equal; the fluid loses more energy when it goes through the filter screen, so the pressure inside the filter screen is relatively smaller.

3.2 Effect of Flow Velocity on Sand Separation Efficiency and Erosion

Considering that the variation of shale gas flow velocity directly affects the sand removal performance and erosion characteristics of the filter desander, the paper makes the simulation analysis of different working conditions with flow velocity ranging from 2 m/s to 18 m/s, as shown in Fig. 9.

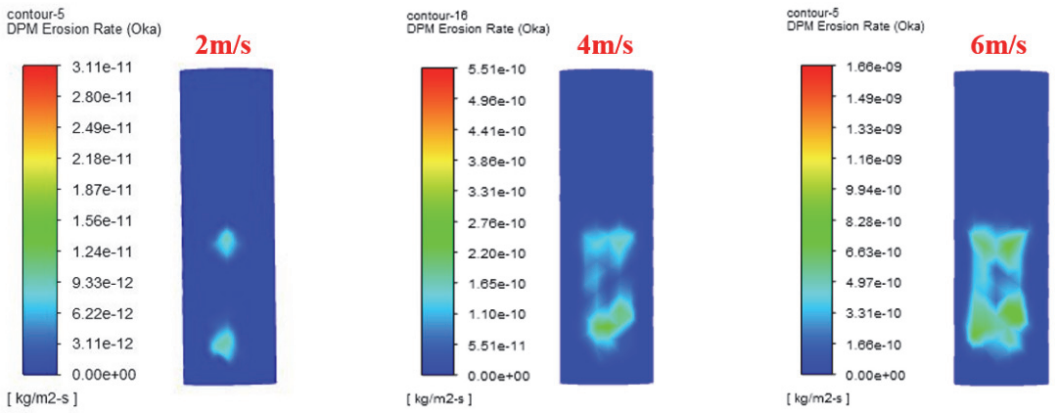

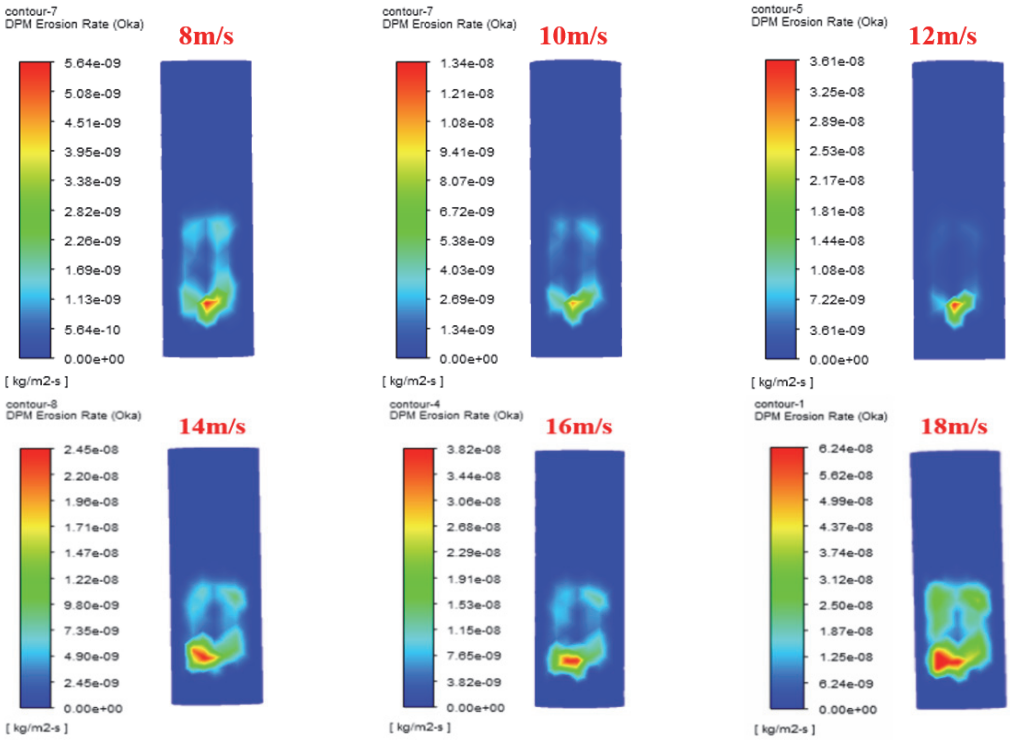

Figure 9 Erosion cloud images of inlet cylindrical baffle at different velocities

The erosion rate at the inlet circular baffle gradually grows as the shale gas velocity increases, and the erosion of the lower part of the baffle is the most obvious. The reason is that the rise in velocity increases the turbulent kinetic energy of sand particles and causes greater erosion wear of the desander wall; and under the influence of gravity, the sand-carrying flow keeps moving downward, so the main erosion area appears in the lower area of the baffle.

Fig. 10 shows the erosion cloud images of the exhaust elbow at different velocities. The erosion of the exhaust elbow mainly occurs at the outer part of the rear half of the elbow, and the erosion also increases with the higher velocity of the shale gas. Compared with the inlet circular baffle, the erosion wear of the exhaust elbow is more serious because the velocity of the outlet pipe section rises [27, 28]. When the shale gas velocity is lower than 8 m/s, the erosion area of the exhaust elbow is relatively small; when the flow velocity is greater than 10 m/s, the erosion area is extended to the outlet of the desander, and the erosion rate increases. Therefore, it is necessary to control the flow velocity within 10 m/s.

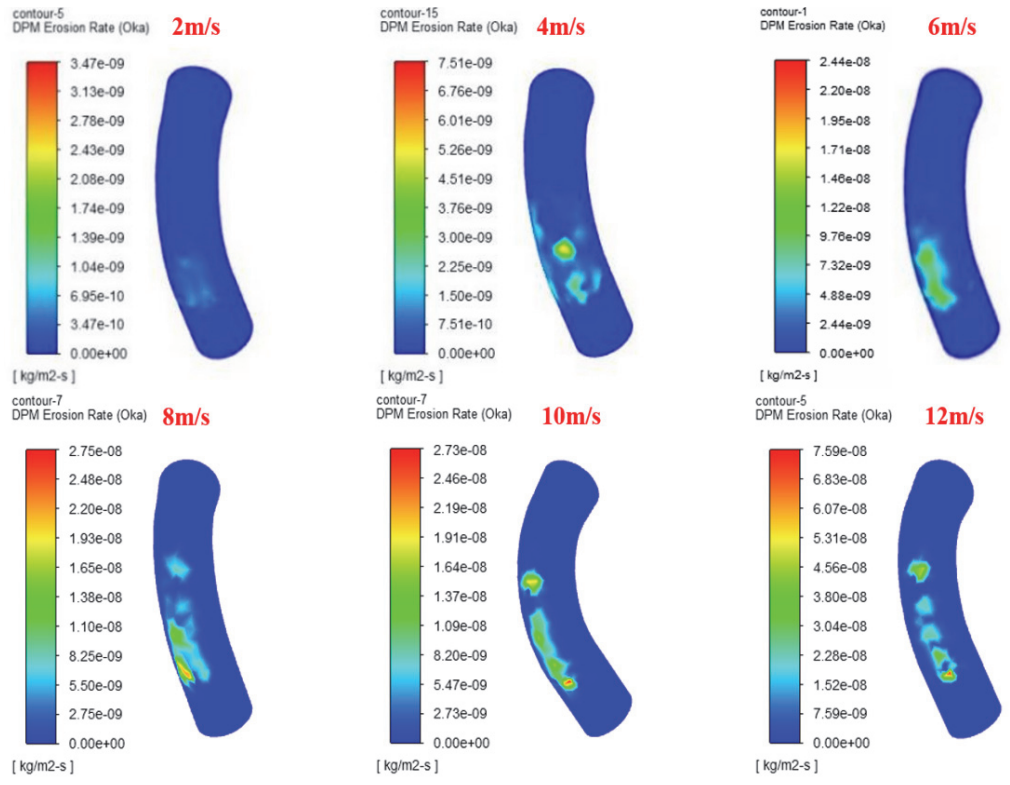

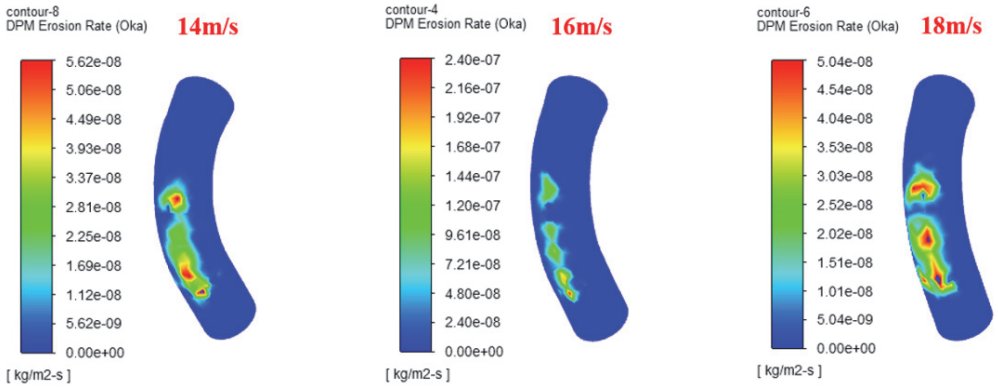

Figure 10 Erosion cloud images of the exhaust elbow at different velocities

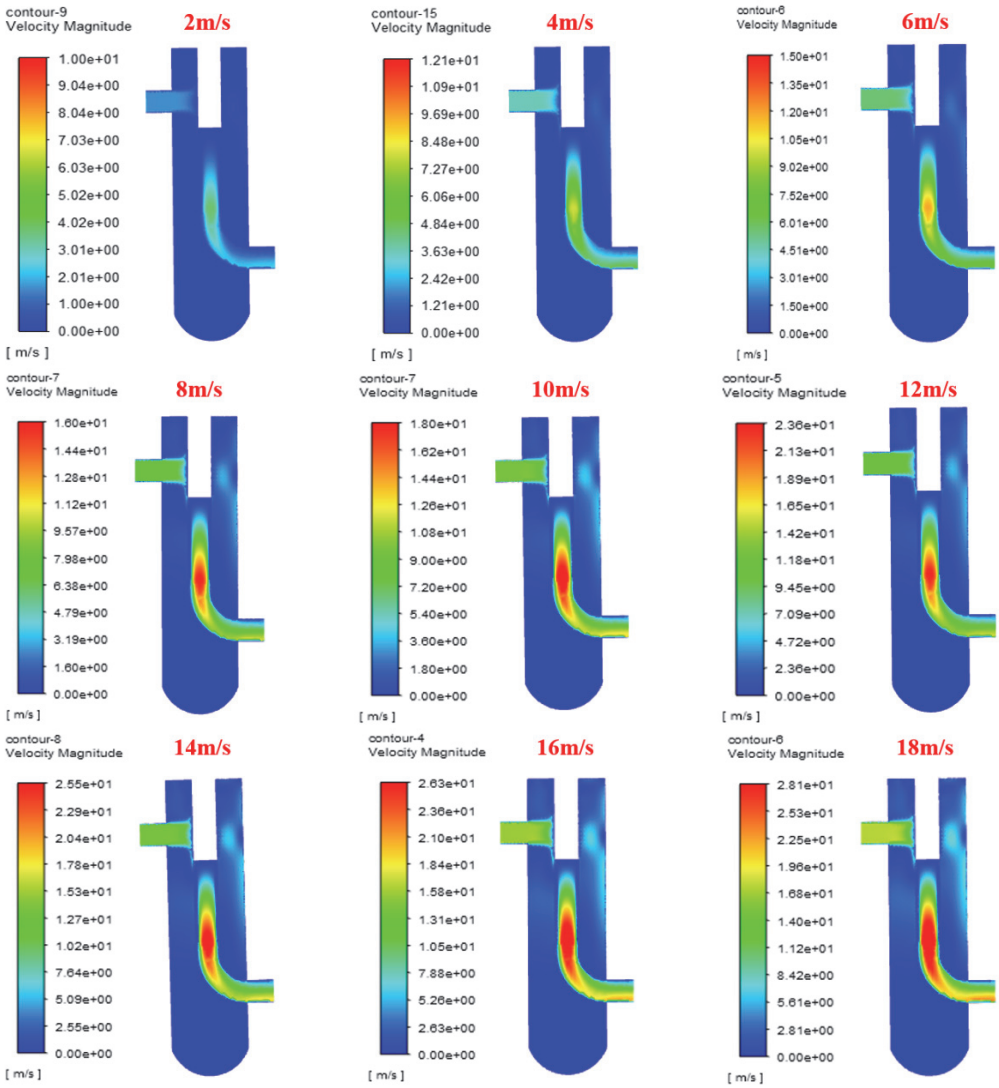

Figure 11 Velocity distribution cloud images of plane 1 at different shale gas velocities

In addition, to further investigate the effect of shale gas velocity on the erosion characteristics of the filter desander, this work also analyzed its velocity field, as shown in Fig. 11.

According to the velocity cloud images at different inlet velocities in Fig. 11, the overall trend of velocity cloud images does not change much as the shale gas velocity increases, indicating that the velocity distribution in the desander is stable. Meanwhile, while the shale gas velocity is greater than 8 m/s, the maximum velocity appears in the filter screen part, and this area expands as the velocity increases. Moreover, this paper extracted the shale gas velocity and turbulent kinetic energy of each data line for quantitative analysis, as shown in Figs. 13 and 14.

Fig. 12 shows the velocity variation curves at different lateral distances, and in the range of 0 to 0.2 m, the velocity first remains constant and then decreases rapidly, while in the range of 0.3 to 0.4 m, the shale gas velocity increases and then decreases [29]. The reason is that the flow direction of the shale gas changes under the action of the circular baffle, and then on the other side of the baffle, the gas converges together again, which is consistent with the regularity of the velocity field in Fig. 7.

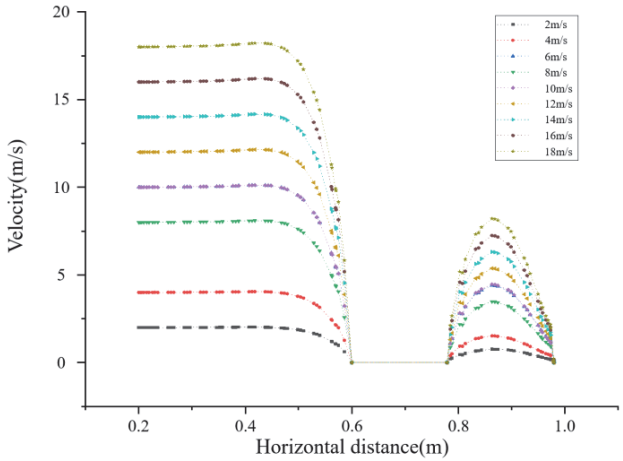

Figure 12 Velocity variation curves at different lateral distances

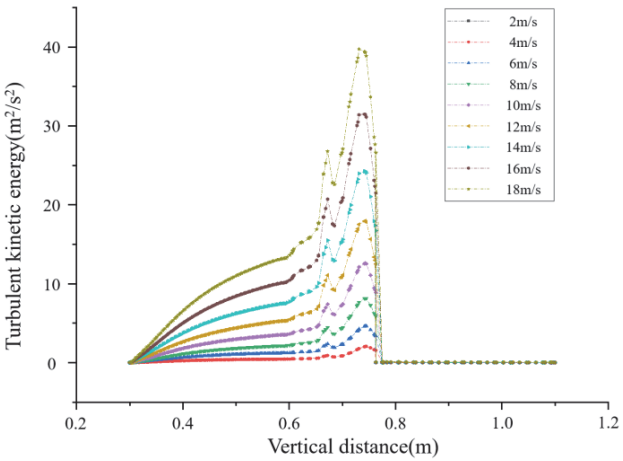

Figure 13 Turbulent kinetic energy variation curves at different vertical distances

As shown in Fig. 13, the turbulent kinetic energy of the shale gas increases with higher flow velocity, which further confirms the previous conclusion. At the inlet circular baffle of the desander, the change in flow velocity does not have a significant effect on the turbulent kinetic energy, but the closer the flow is to the bottom of the desander, the higher the peak turbulent energy of the fluid in the high flow velocity condition, which leads to increased erosion. In addition, the erosion simulation conditions based on shale gas desander are also applicable to the numerical study of the desanding performance, so the separation efficiency of the desander was also studied, as shown in Fig. 14.

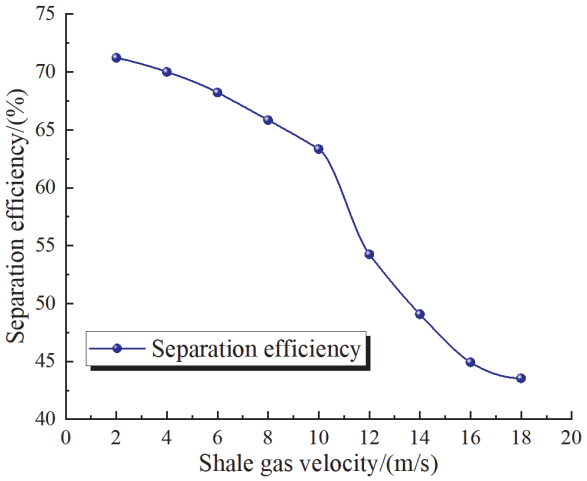

Figure 14 Sand removal efficiency at different shale gas velocities

Fig. 14 indicates that the sand removal efficiency decreases gradually with the increase of shale gas velocity. When the inlet velocity is less than 8 m/s, the sand removal efficiency of the desander is high and decreases slowly, because the energy contained in the solid particles is low at this time, so it is easy to be caught by the dust outlet under the influence of gravity. When the inlet velocity is greater than 10 m/s, it is easier for the solid particles to escape from the desander due to the higher flow velocity and larger energy of the particles.

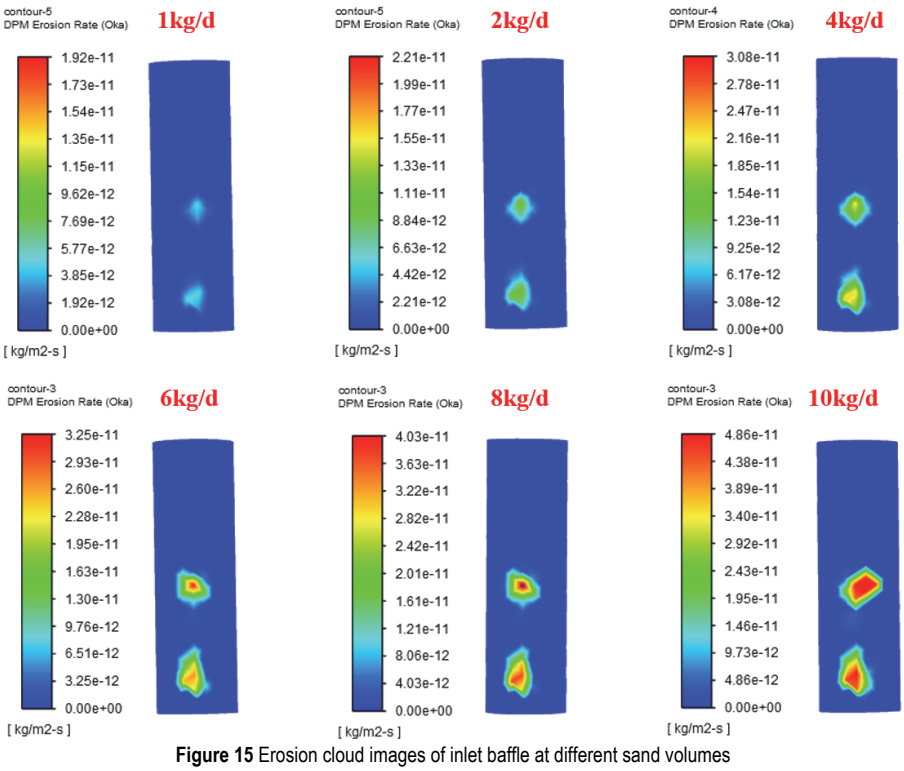

Figure 15 Erosion cloud images of inlet baffle at different sand volumes

3.3 The Effect of Sand Content on Sand Particle Separation Efficiency and Erosion

Since the sand production rate in each stage of the shale gas field production is constantly changing, it is necessary to analyze and discuss the sand removal performance and erosion characteristics of the desander under different sand volumes. The following simulations and analyses were conducted under the operating condition of shale gas velocity of 6 m/s and sand volume of 1 to 10 kg/d, as shown in Fig. 15.

The sand-carrying flow entering the desander is affected by the flow field fluctuation, resulting in irregular ring-shaped erosion on the inlet circular baffle. When the sand volume is 1 kg/d, the erosion characteristics of the circular baffle are not obvious, and the erosion area follows a point distribution. As the sand mass flow increases, the erosion rate of the circular baffle gradually increases [30].

Fig. 16 shows the erosion cloud images of the exhaust elbow at different sand volumes. The main erosion area of the exhaust elbow is the bottom half of the elbow, and the erosion area keeps extending toward the outlet as the sand volume increases. Since the sand particles are affected by gravity, they mainly impact the bottom of the exhaust elbow when they follow the gas to escape from the exhaust port.

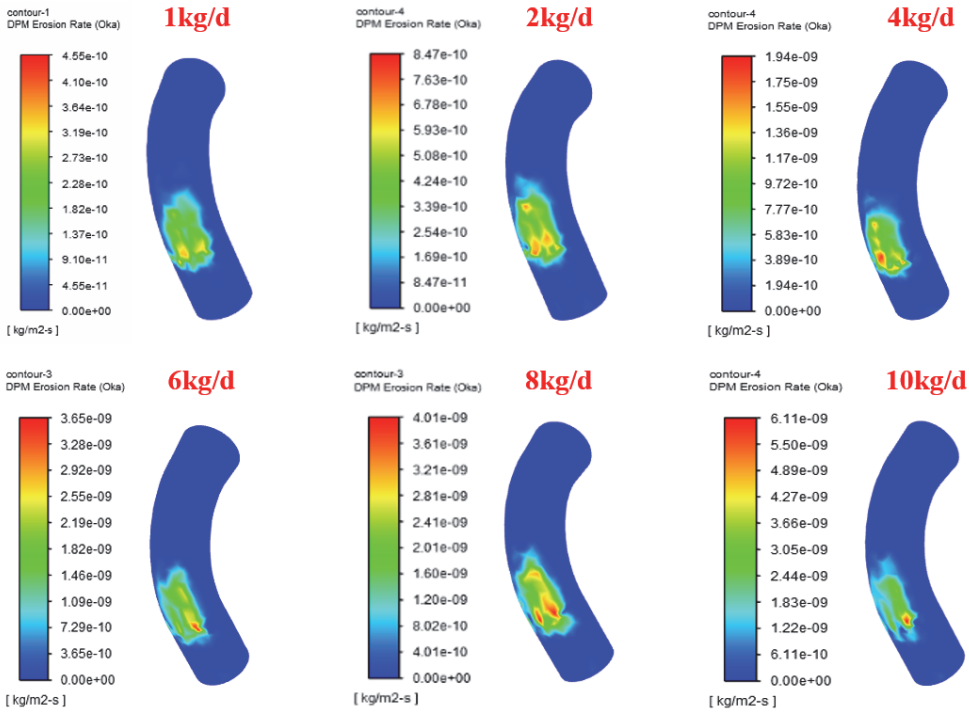

Figure 16 Erosion cloud images of the exhaust elbow at different sand volumes

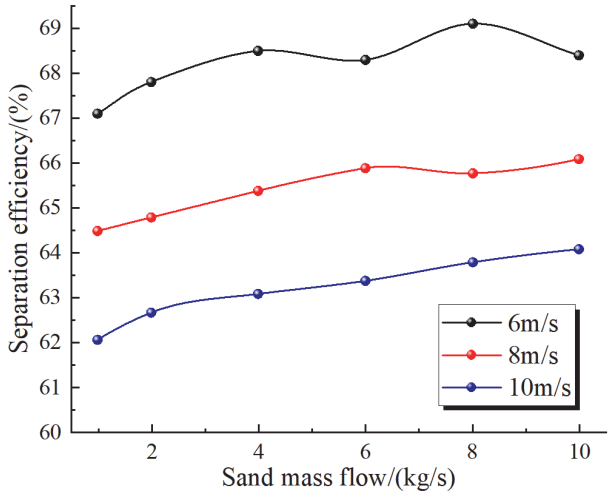

Figure 17 Sand removal efficiency at different sand mass flow rates

Fig. 17 shows the sand removal efficiency at three inlet velocities with different sand volumes. When the velocity of shale gas is constant, the sand mass flow rate has a small effect on the sand removal performance of the desander. While the velocity changes from 6 m/s to 10 m/s, the decrease in sand removal efficiency is almost always above 5% under a certain sand mass flow rate.

3.4 Effect of Sand Particle Size on Sand Separation Efficiency and Erosion

The size of sand particles from the extracted gas varies and affects the variation of the erosion characteristics and sand removal performance of the filter desander. Therefore, the paper studied the sand removal performance and erosion characteristics of different sand sizes (10 to 100 μm), as shown in Fig. 18.

The erosion rate at the circular baffle gradually increases with the larger sand size. When the sand size is less than 50 μm, the erosion area of the circular baffle is distributed in the two upper and lower clumps, and the maximum erosion appears as a dot. Moreover, the erosion area on the circular baffle gradually integrates into a whole when the sand size is larger than 50 μm. When the sand size is 100 μm, due to the large inertia of the sand particles, the influence of the internal flow field of the desander is smaller than the influence of their own inertia, so there are several obvious erosion points on the baffle.

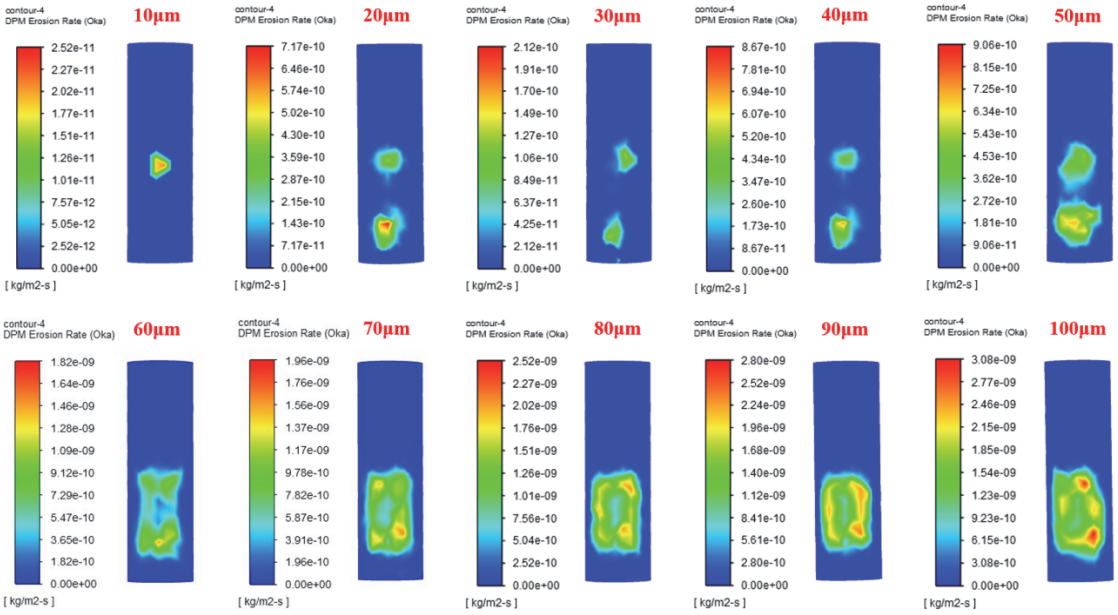

Figure 18 Erosion cloud images of inlet baffle under different sand sizes

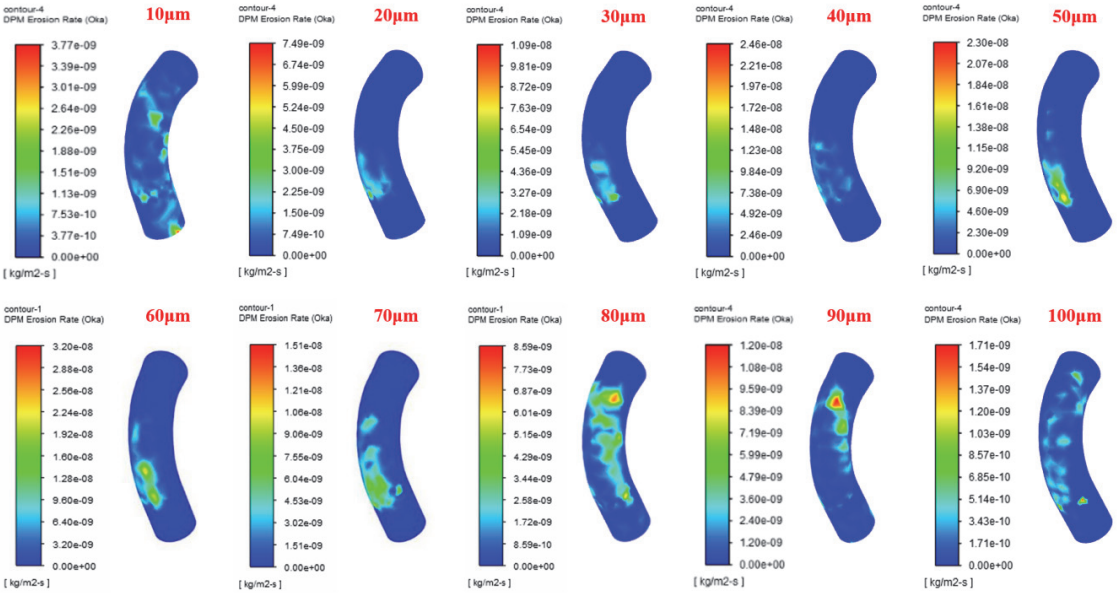

Figure 19 Erosion cloud images of exhaust elbow under different sand sizes

Fig. 19 shows the erosion cloud images of the exhaust elbow under different particle sizes. As the sand diameter increases, the erosion rate at the exhaust elbow grows. When the sand size is 10 μm, the erosion area is distributed both inside and outside of the elbow. When the sand size is in the range of 20 ~ 70 μm, the erosion area is concentrated on the outside of the elbow and the erosion is gradually strengthened, and the major erosion area migrates downward. But when the sand size is greater than or equal to 80 μm, the major erosion areas in the exhaust elbow gradually migrate upward. In addition, to quantify the sand removal performance of the shale gas desander under different particle sizes, the paper extracted the separation efficiency under each operating condition, as shown in Fig. 20.

As the sand size increases, the overall sand removal efficiency shows a linear growth trend. The larger the sand size, the better the separation effect. When the sand size is 10 μm, the sand removal efficiency of the desander is 37%. And the sand removal efficiency is close to 85% when the sand size increases to 100 μm, which is an increase of 2.3 times.

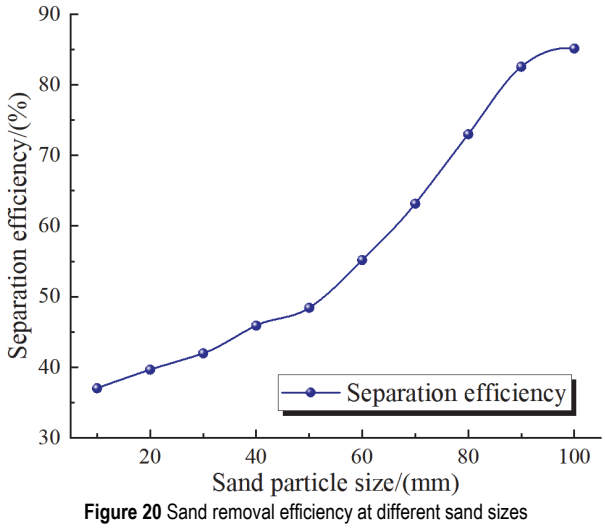

Figure 20 Sand removal efficiency at different sand sizes

3.5 Effect of Desander Pressure on Sand Separation Efficiency and Erosion

Through the field study of the Sichuan shale gas field, it was found that the pressure of shale gas varies greatly, and the pressure of desander can affect the physical properties of shale gas based on Basyouny's study, resulting in fluctuation of sand removal efficiency. Therefore, this paper also analyzes the sand removal performance and erosion characteristics of shale gas vertical desanders under different operating pressures (1 to 6 MPa), as shown in Fig. 21.

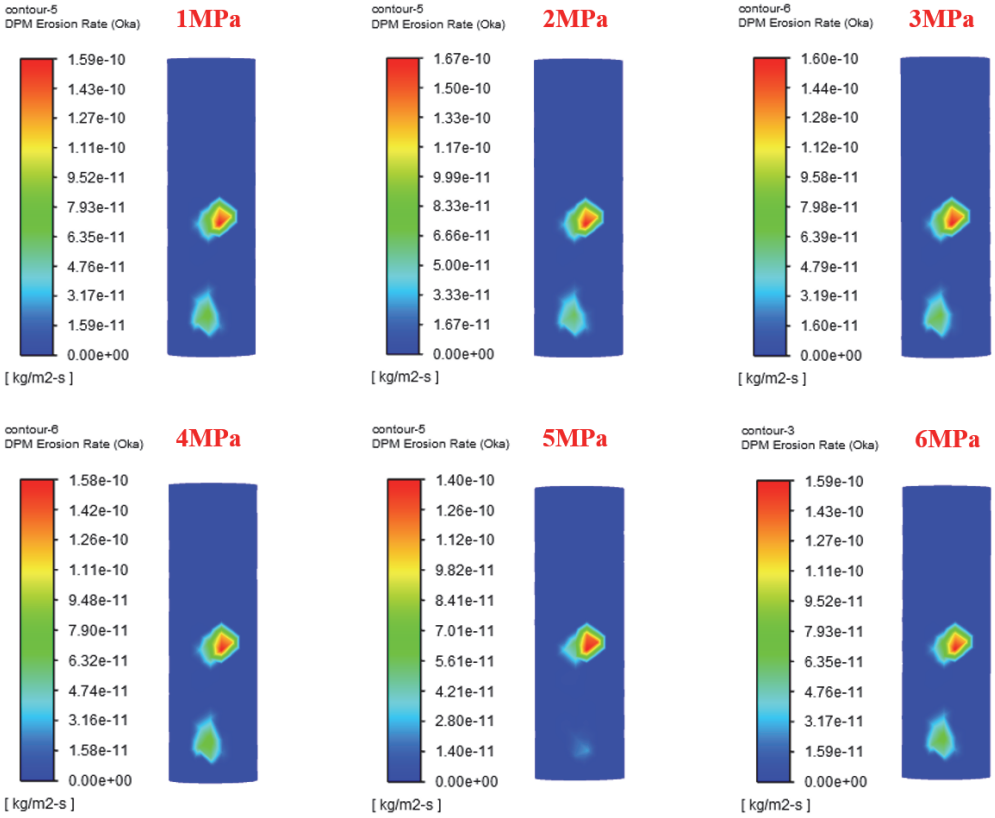

Figure 21 Erosion cloud images of inlet baffle at different operating pressures

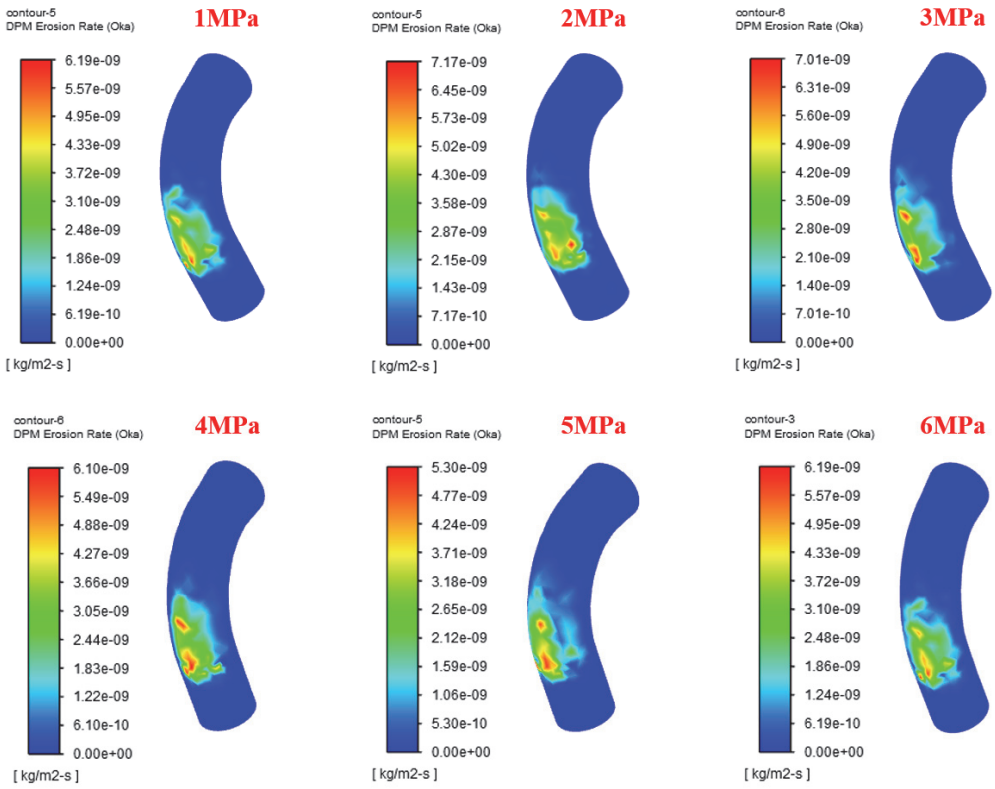

Figure 22 Erosion cloud images of exhaust elbow at different operating pressures

The erosion area of the circular baffle mainly is distributed in dots when the pressure varies from 1 to 6 MPa, and the lower part of the baffle is also affected by the erosion wear of sand particles. However, the pressure increase of the desander does not cause the erosion area of the circular baffle to change significantly. With the growth of operating pressure, the degree is also very limited although the erosion rate of the circular baffle increases.

Fig. 22 shows the erosion cloud images of the exhaust elbow at different operating pressures. When the operating pressure increases from 1 to 6 MPa, the erosion of the exhaust elbow is relatively stable, and the erosion area is mainly concentrated in the outer part of the lower half of the elbow. However, with the change in operating pressure, the flow field of the desander does not show obvious fluctuation, and the erosion wear of solid sand particles on the elbow is also relatively stable.

4 CONCLUSION

(1) When the sand-carrying flow meets the circular baffle, the flow velocity decreases, and some sand particles are separated from the gas. After bypassing the circular baffle, the dispersed gas flow gathers again on the other side of the baffle, and reentry movement occurs. In addition, when the velocity rises, the erosion wear of both the circular baffle and the exhaust elbow increases and the separation efficiency decreases. This is especially obvious when the flow velocity exceeds 10 m/s, so it is necessary to control the flow velocity within 10 m/s.

(2) The change in sand mass flow rate and operating pressure has a small effect on the sand removal performance of the filter desander. However, as the sand volume increases, the erosion rate increases, and the erosion area expands. Compared with the above two factors, the change in sand particle size has a greater impact on the sand removal performance and erosion characteristics of the desander. When the sand size increases from 10 to 100 μm, the erosion area of the filter desander changes from point distribution to sheet-like distribution, and the separation efficiency grows to 85%.

(3) The corrosion resistance of the existing filter desander needs to be further improved. It is suggested to improve the entrance structure of the desander, reduce the impact angle, improve the sand removal efficiency, and reduce the erosion rate. Due to workload limitations, this paper did not analyze the combined effects of multiple factors. In the future, an evaluation of the filter desander can be conducted around this aspect.

Acknowledgements

This work was supported by the Sichuan Natural Science Foundation (2023NSFSC0422).

5 REFERENCES

[1] Al-Abboodi, N. K. F. & Ridha, H. (2023). Review of Compression Ignition Engine Powered by Biogas and Hydrogen. *Power Engineering and Engineering Thermophysics*, *2*(2), 57-72. https://doi.org/10.56578/peet020201

[2] Liu, E., Li, D., Zhao, W., Peng, S., & Chen, Q. (2022). Correlation analysis of pipeline corrosion and liquid accumulation in gas gathering station based on computational fluid dynamics. *Journal of Natural Gas Science and Engineering*, *102*, 104564. https://doi.org/10.1016/j.jngse.2022.104564

[3] Agarwal, A. (2023). Heat Absorption Performance Enhancement of TES System Using Iron Oxide/Paraffin Wax Composite. *Power Engineering and Engineering Thermophysics*, *2*(2), 73-85. https://doi.org/10.56578/peet020202

[4] Zou, C., Zhao, Q., Cong, L., Wang, H., Shi, Z., Wu, J., & Pan, S. (2021). Development progress, potential and prospect of shale gas in China. *Natural Gas Industry*, *41*(1), 1-14.

[5] Liu, E., Li, D., Li, W., Liao, Y., Qiao, W., Liu, W., & Azimi, M. (2021). Erosion simulation and improvement scheme of separator blowdown system-A case study of Changning national shale gas demonstration area. *Journal of Natural Gas Science and Engineering*, *88*, 103856. https://doi.org/10.1016/j.jngse.2021.103856

[6] Feng, D., Ruan, C., Liu, X., Wamg, P., & Zhang, H. (2012). The research of heating furnace with heavy oil desander. *Energy Procedia*, *14*, 674-680. https://doi.org/10.1016/j.egypro.2011.12.994

[7] Hwang, K. J., Hwang, Y. W., & Yoshida, H. (2013). Design of novel hydrocyclone for improving fine particle separation using computational fluid dynamics. *Chemical Engineering Science*, *85*, 62-68. https://doi.org/10.1016/j.ces.2011.12.046

[8] Zhang, J., Zha, Z., Che, P., Ding, H., & Pan, W. (2019). Influences of inlet height and velocity on main performances in the cyclone separator. *Particulate Science and Technology*, *37*(6), 669-676. https://doi.org/10.1080/02726351.2018.1423589

[9] Masoumeh, M., Shuran, L., Qinzhen, Z., Guanle, D., Zhen, L., & Keping, Y. (2019). Performance evaluation of a new micro gas cyclone using simulation and experimental studies to capture indoor fine particles. *Advanced Powder Technology*, *30*(6), 1151-1159. https://doi.org/10.1016/j.apt.2019.03.010

[10] Alves, D. G., da Silva, J. T. T., Quintino, D. B., & Ataíde, C. H. (2020). Desander mini-hydrocyclones applied to the separation of microspheres and sand in non-Newtonian fluid: Efficiencies and drag analysis. Separation and Purification Technology, *234*, 116131. https://doi.org/10.1016/j.seppur.2019.116131

[11] Peng, S., Li, M., & Zhang, Y. (2020). Study on gas solid two phase separation characteristics of shale gas desander for manufacturing industry. *Manufacturing Automation*, *42*(12), 138-142.

[12] Basyouny, A. (2022). Sand settling in a three-phase flow inside a horizontal separator. *International Journal of Thermofluids*, *16*, 100235. https://doi.org/10.1016/j.ijft.2022.100235

[13] Morales, P. V., Gómez, D. E., Vega, A. P., & Nieto, F. M. (2023). Modeling and simulation in CFD of mercury contamination in the city of Guanajuato, Mexico. *Environmental and Earth Sciences Research Journal*, *10*(1), 1-6. https://doi.org/10.18280/eesrj.100101

[14] Liu, E. B., Peng, Y., Peng, S. B., Yu, B., & Chen, Q. K. (2022). Research on low carbon emission optimization operation technology of natural gas pipeline under multi-energy structure. *Petroleum Science*, *19*(6), 3046-3058. https://doi.org/10.1016/j.petsci.2022.09.025

[15] Yang, T., Hong, Y., Wang, A. J., Ran, X. F., Fan, X. J., & Hu, C. P. (2021). Failure mechanism and optimization of throttle valve based on computational fluid dynamics. *International Journal of Heat and Technology*, *39*(3), 906-912. https://doi.org/10.18280/ijht.390325

[16] Sedrez, T. A., Decker, R. K., da Silva, M. K., Noriler, D., & Meier, H. F. (2017). Experiments and CFD-based erosion

modeling for gas-solids flow in cyclones. *Powder Technology*, *311*, 120-131. https://doi.org/10.1016/j.powtec.2016.12.059

[17] Tofighian, H., Amani, E., & Saffar-Avval, M. (2020). A large eddy simulation study of cyclones: The effect of sub-models on efficiency and erosion prediction. *Powder Technology*, *360*, 1237-1252. https://doi.org/10.1016/j.powtec.2019.10.091

[18] Liu, E., Tian, D., Li, W., Chen, J., & Chen, Q. (2021). Study on erosion behavior and separation efficiency of a shale gas vertical separator. *Energy & Fuels*, *35*(5), 3878-3886. https://doi.org/10.1021/acs.energyfuels.0c03979

[19] Liu, E., Kou, B., Wu, P., Wang, M., Peng, J., & Chen, Q. (2022). Performance analysis and structure optimization of shale gas desander. *Energy Sources, Part A: Recovery, Utilization, and Environmental Effects*, 1-21. https://doi.org/10.1080/15567036.2022.2040656

[20] Liu, G., Wang, W., Yu, J., & Li, X. (2022). Effect of extra inlets structure on cyclone wall erosion. *Powder Technology, 411*, 117926. https://doi.org/10.1016/j.powtec.2022.117926

[21] Zhang, L., Fan, J., Zhang, P., Gao, F., Chen, G., & Li, J. (2023). Effect of local erosion on the flow field and separation performance of the cyclone separator. *Powder Technology*, *413*, 118007. https://doi.org/10.1016/j.powtec.2022.118007

[22] Su, Z., Liu, E., Xu, Y., Xie, P., Shang, C., & Zhu, Q. (2019). Flow field and noise characteristics of manifold in natural gas transportation station. *Oil & Gas Science and Technology - Revue d'IFP Energies nouvelles*, *74*, 70. https://doi.org/10.2516/ogst/2019038

[23] Chen, Y., Fu, W., & Deng, H. (2020). Central tube erosion investigation of torque impactor in the deep shale gas formation. *Energy Sources, Part A: Recovery, Utilization, and Environmental Effects*, 1-15. https://doi.org/10.1080/15567036.2020.1732504

[24] Peng, S., Chen, Q., & Liu, E. (2020). The role of computational fluid dynamics tools on investigation of pathogen transmission: Prevention and control. *Science of The Total Environment*, *746*, 142090. https://doi.org/10.1016/j.scitotenv.2020.142090

[25] Oka, Y. I., Okamura, K., & Yoshida, T. (2005). Practical estimation of erosion damage caused by solid particle impact: Part 1: Effects of impact parameters on a predictive equation. *Wear*, *259*(1-6), 95-101. https://doi.org/10.1016/j.wear.2005.01.039

[26] Messa, G. V. & Malavasi, S. (2017). The effect of sub-models and parameterizations in the simulation of abrasive jet impingement tests. *Wear*, *370*, 59-72. https://doi.org/10.1016/j.wear.2016.10.022

[27] Zhou, H., Ji, Q., Liu, W., Ma, H., Lei, Y., & Zhu, K. (2022). Experimental study on erosion-corrosion behavior of liquid-solid swirling flow in pipeline. *Materials & Design*, *214*, 110376. https://doi.org/10.1016/j.matdes.2021.110376

[28] Zhou, H., Zhang, Y., Ma, H., Lei, Y., Yang, Z., Zhao, H., ... & Zhu, K. (2023). Inhibition of the erosion-corrosion of elbow by synergistic action of swirling flow and inhibitor. *Wear*, *514*, 204570. https://doi.org/10.1016/j.wear.2022.204570

[29] Zhou, H., Zhang, Y., Bai, Y., Zhao, H., Lei, Y., Zhu, K., & Ding, X. (2021). Study on reducing elbow erosion with swirling flow. *Colloids and Surfaces A: Physicochemical and Engineering Aspects*, *630*, 127537. https://doi.org/10.1016/j.colsurfa.2021.127537

[30] Peng, S., Zhang, Y., Zhao, W., & Liu, E. (2021). Analysis of the influence of rectifier blockage on the metering performance during shale gas extraction. *Energy & Fuels*, *35*(3), 2134-2143. https://doi.org/10.1021/acs.energyfuels.0c03748

Contact information:

Jian ZHANG, Engineer
Safety, Environment and Technology Supervision Research Institute of Southwest Oil and Gas Field Company,
Chengdu 610000, Sichuan, China
E-mail: z_jian@petrochina.com.cn

Chang LIU, Senior Engineer
Safety, Environment and Technology Supervision Research Institute of Southwest Oil and Gas Field Company,
Chengdu 610000, Sichuan, China
E-mail: liuchang02@petrochina.com.cn

Dong LIN, Senior Engineer
Safety, Environment and Technology Supervision Research Institute of Southwest Oil and Gas Field Company,
Chengdu 610000, Sichuan, China
E-mail: lin_dong@petrochina.com.cn

Jian GAO, Senior Engineer
Safety, Environment and Technology Supervision Research Institute of Southwest Oil and Gas Field Company,
Chengdu 610000, Sichuan, China
E-mail: gao.jian@petrochina.com.cn

Changchao QI, Senior Engineer
Safety, Environment and Technology Supervision Research Institute of Southwest Oil and Gas Field Company,
Chengdu 610000, Sichuan, China
E-mail: qichangchao@petrochina.com.cn

Jun JIANG, Engineer
Chongqing Gas Mine of Southwest Oil and Gas Field Company,
Chongqing 400707, China
E-mail: jiang.jun@petrochina.com.cn

Bo KOU, Master Degree Candidate
Southwest Petroleum University,
Petroleum Engineering School,
Chengdu 610500, China
E-mail: 1044595028@qq.com

Shanbi PENG, Professor
(Corresponding author)
Southwest Petroleum University,
School of Civil Engineering and Geomatics,
Chengdu 610500, China
E-mail: shanbipeng@gmail.com